

Ultrahigh-Temperature Ceramic Aerogels

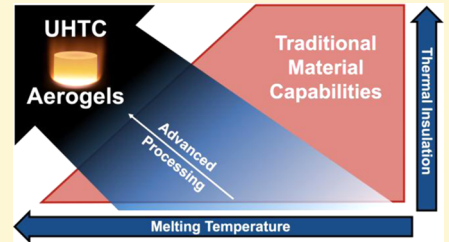
James T. Cahill,^{†,‡,§,||,ID} Sally Turner,^{†,‡,§,||,ID} Jianchao Ye,^{†,ID} Brian Shevitski,^{‡,⊥} Shaul Aloni,^{‡,⊥} Theodore F. Baumann,[†] Alex Zettl,^{‡,||,#} Joshua D. Kuntz,[†] and Marcus A. Worsley^{*,†}

[†]Physical and Life Sciences Directorate, Lawrence Livermore National Laboratory, Livermore, California 94551, United States

[‡]Physics Department, [§]Chemistry Department, and ^{||}Kavli Energy NanoSciences Institute, University of California, Berkeley, California 94720, United States

[#]The Molecular Foundry and [#]Materials Sciences Division, Lawrence Berkeley National Laboratory, Berkeley, California 94720, United States

ABSTRACT: We demonstrate the synthesis of high-surface-area, low-density refractory aerogels. The monolithic hafnium boride (HfB_2) and zirconium boride (ZrB_2) aerogels are prepared via borothermal reduction of precursor hafnia and zirconia aerogels, respectively, consisting of a fine mixture of boron nanoparticles and the metal oxide. This precursor boron–metal oxide ($\text{B}-\text{MO}_2$) composite aerogel was synthesized by modifying the pure ethanol solvent typically used in the epoxide-initiated sol–gel synthesis of metal oxide aerogels with an ethanolic boron nanoparticle suspension. After reduction, precursor aerogels are converted to metal boride aerogels containing primary particles in the sub-100 nm regime. The relative densities of the HfB_2 and ZrB_2 aerogels are 3 and 7%, respectively, and could be tailored by simply changing the density of the precursor aerogels via modifying the reagent concentrations or the drying conditions. Thermal conductivities of the ZrB_2 monoliths ranged from 0.18 to 0.33 W/(m K). The surface areas of the HfB_2 and ZrB_2 aerogels were 10 and 19 m²/g, respectively. Successful reduction of the aerogels to the diboride phase was confirmed by X-ray diffraction.



INTRODUCTION

Ultrahigh-temperature ceramics (UHTC) such as hafnium boride and zirconium boride possess a number of extraordinary qualities. They exhibit extremely high melting temperatures (>3000 °C),¹ good thermal oxidation resistance,^{2–4} robust mechanical properties at elevated temperatures^{5–7} and are electrically conductive.^{8–10} As such, UHTCs have proven effective in applications that involve extreme conditions, like plasma-arc electrodes¹¹ or heat shielding in hypervelocity reentry vehicles.^{12,13} However, metal borides also possess good thermal conductivity,^{8,14–16} which is disadvantageous for insulation applications. Aerogels, on the other hand, exhibit some of the lowest thermal conductivity values recorded^{17–19} but primarily consist of metal oxides, which have melting points substantially lower than those of their metal boride counterparts, or carbon, which is limited to oxygen-free environments. Although aerogels of transition-metal oxides (such as ZrO_2 and HfO_2) have been previously synthesized,^{20–24} prior art^{25–28} in the synthesis of these metal boride materials has been focused on powders or medium-density (50–70% porous) solids with relatively large (~1 μm) grains.

In this communication, we describe the synthesis of low-density HfB_2 and ZrB_2 aerogels with submicron grains via borothermal reduction of boron–metal oxide ($\text{B}-\text{MO}_2$) precursor aerogels. Critical to producing a monolithic metal diboride aerogel is the three-dimensional (3D) assembly of the $\text{B}-\text{MO}_2$ precursor aerogel, which must be assembled with a homogeneous distribution of both components at a fine scale such that the 3D aerogel structure can be maintained through

the drying and borothermal reduction processes. The sol–gel synthesis technique intimately mixes the boron and metal oxide at the smallest scale and creates a homogeneous distribution of interconnected metal-oxide-coated boron nanoparticles. The versatile nature of sol–gel synthesis and the reduction process allow for the production of a wide variety of metal borides and carbides in low-density forms similar to the results presented here.

EXPERIMENTAL METHODS

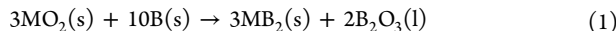
Aerogel Preparation. In a typical synthesis, the preparation of the ethanolic boron nanoparticle suspension was accomplished by dispersing 5 wt % 30 nm boron (Specialty Materials, Inc.) in 200 proof ethanol via tip sonication and planetary mixing. If desired, the density of the final gel can be tailored by adjusting the wt % of suspended boron nanoparticles. $\text{B}-\text{MO}_2$ precursor aerogels are prepared by combining the suspension with deionized water and the corresponding metal chloride (M) at a molar ratio of 34:1 H₂O/M, boron (B) at a molar ratio of 10:1 B/M, and propylene oxide (PO) at a molar ratio of 9:1 PO/M. A typical $\text{B}-\text{MO}_2$ precursor aerogel is synthesized by adding either hafnium tetrachloride (Sigma-Aldrich 98%) or zirconium tetrachloride (Sigma-Aldrich 99.9%) and water to the ethanolic boron suspension. This suspension is chilled to 0 °C before adding the propylene oxide (Sigma-Aldrich 99%) while stirring. Gelation occurs in a matter of minutes, followed by acetone washing before drying. Drying of the gels can be accomplished via critical point drying (aerogels) or ambient drying (xerogels). Little to

Received: February 1, 2019

Revised: April 30, 2019

Published: May 13, 2019

no shrinkage is observed for critical point drying, and linear shrinkage of up to 50% was observed if dried under ambient conditions. Borothermal reduction was performed in a graphite furnace (Thermal Technologies) under flowing helium. The precursor aerogels were first ramped at 2 °C/min to 1050 and 1150 °C for B–ZrO₂ and B–HfO₂, respectively, held for 2 h, then ramped at 10 °C/min to 1600 °C, and held for 1 h before cooling to room temperature. The borothermal reduction of ZrO₂ and HfO₂ proceeds at 1000 and 1100 °C, respectively, as per the following reaction



where M = Hf or Zr. Following the work of Guo et al., a subsequent anneal at 1600 °C was used to vaporize the boron oxide (melting point = 450 °C) byproduct²⁶



Characterization. Field emission scanning electron microscopy (FE-SEM) was performed on JEOL 7401-F at 5–10 keV (20 mA) in lower secondary electron imaging mode with a working distance of 2–8 mm. Transmission electron microscopy (TEM) characterization was performed on a JEOL 2010 electron microscope operated at 80 kV. Thermal constants were measured using a thermttest hot disk TPS 3500 with a double-sided 0.888 mm radius TPS sensor. Aerogel and xerogel samples were right cylinders between 2 and 4 mm thick and 10 mm in diameter. Measurements were taken in the power and time range of 5–10 mW and 0.2–1 s, respectively. Textural properties were determined by the Brunauer–Emmett–Teller (BET) and Barrett–Joyner–Halenda methods using an ASAP 2020 surface area analyzer (Micromeritics Instrument Corporation) via nitrogen porosimetry.²⁹ Samples of approximately 0.1 g were heated to 150 °C under vacuum (10–5 Torr) for at least 24 h to remove all adsorbed species. X-ray diffraction (XRD) measurements were performed on a Bruker AXS D8 ADVANCE X-ray diffractometer scanning from 10 to 80° 2θ with 0.02° steps and 2 s dwell. Phases in the samples were identified by the comparison of observed peaks to those in the International Centre for Diffraction Data (ICDD PDF2018) powder diffraction database and listed in reference articles. Indentation was performed using an MTS Nanoindenter XP with a 50 μm spherical sapphire tip and a maximum load of 15 mN. Young's modulus and hardness were extracted using the Oliver and Pharr method with a penetration depth of 5 μm. Bulk densities of the samples were determined from the physical dimensions and mass.

RESULTS AND DISCUSSION

Figure 1 shows the scheme used to synthesize the metal diboride aerogels. The supercritically dried B–MO₂ samples

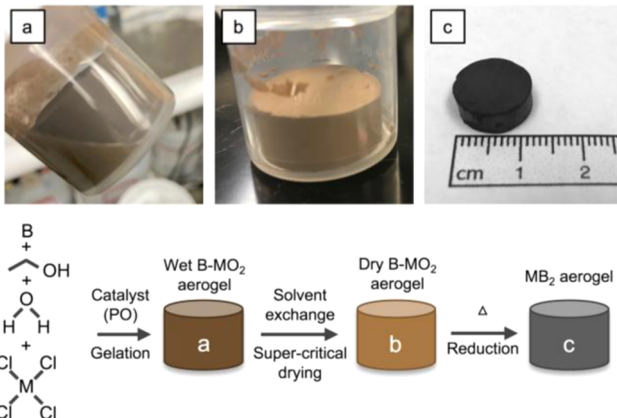


Figure 1. Typical aerogel synthesis in which (a) boron is suspended in ethanolic metal salt solution before adding propylene oxide to produce the wet B–MO₂ gel, followed by (b) supercritical drying and (c) high-temperature annealing to form the final MB₂ aerogel.

(Figure 1b) display little to no shrinkage from the gelled state (Figure 1a). After supercritical drying, electron microscopy provides a detailed view of the porous framework that constitutes the B–MO₂ precursor aerogels. SEM images in Figure 2 show that the primary particle size of the precursor

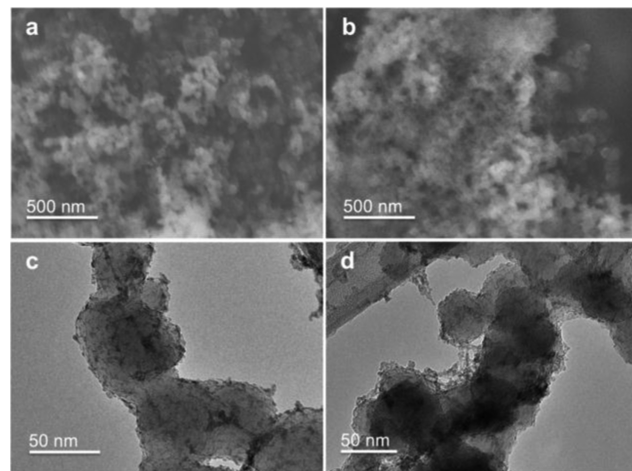


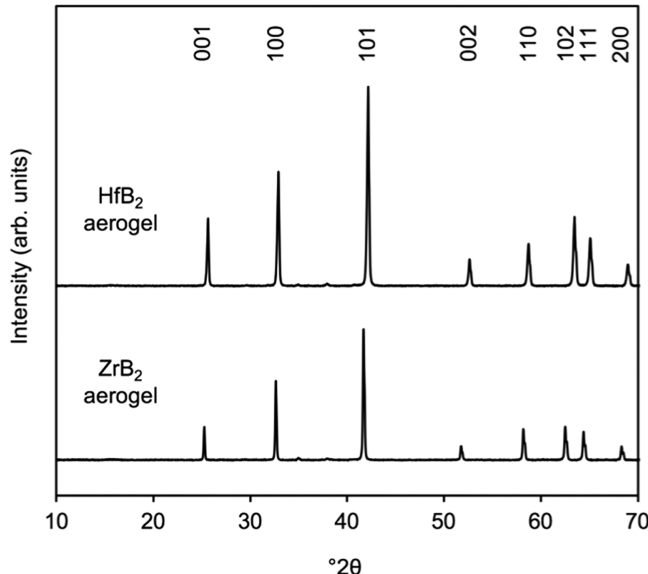
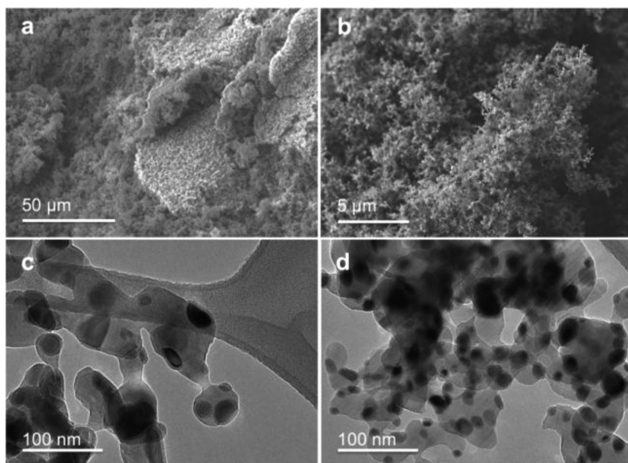
Figure 2. SEM images of (a) boron nanopowder and (b) B–ZrO₂ aerogel precursor. TEM images of (c) B–ZrO₂ and (d) B–HfO₂ aerogel precursors.

aerogel (Figure 2b) is similar to that of the boron nanoparticles (Figure 2a), e.g., sub-100 nm, and the network structure of the precursor aerogel closely resembles that of the boron nanopowder. TEM (Figure 2c,d) confirms that the primary particle network in the precursor aerogel consists of boron nanoparticles coated and cross-linked by the much finer ZrO₂ or HfO₂ nanoparticles. These results confirm that a homogeneous, finely distributed mixture of boron and metal oxide was achieved in the precursor aerogel. After firing the B–ZrO₂ and B–HfO₂ aerogels, the monoliths have changed color from brown to gray and shrunk uniformly (ca. 30–40% linear shrinkage), maintaining their original shape (Figure 1C). The densities of the ZrB₂ and HfB₂ aerogels (supercritical drying) and xerogels (ambient drying) are listed in Table 1. Confirmation of a complete borothermal reduction was determined by XRD, as shown in Figure 3, where the diffraction peaks observed in the spectra from the ZrB₂ and HfB₂ aerogels are consistent with those expected for bulk ZrB₂ (PDF 00-034-0423) and HfB₂ (PDF 00-038-1398), respectively. No peaks corresponding to oxide, boron, or metal impurities were observed, indicating that full reduction of the B–MO₂ precursor aerogels to MB₂ aerogels was achieved.

The two low-intensity peaks at 35 and 38° 2θ represent a small amount of B₄C that has formed from contact with the graphite crucible during reduction. Analysis of the peaks using the Scherrer equation indicates that the average crystallite sizes were calculated to be approximately 43 and 37 nm for ZrB₂ and HfB₂ aerogels, respectively. Electron microscopy was performed on the ZrB₂ and HfB₂ aerogels to characterize pore morphology after borothermal reduction. SEM (Figure 4a,b) suggests that the distribution of primary particle sizes of the ZrB₂ and HfB₂ aerogels has widened compared to the precursor aerogel. Some larger (100–200 nm) particles are now present in the ZrB₂ and HfB₂ aerogels, though the majority of the particles are still less than 100 nm. TEM (Figure 4c,d) also shows that though there is a population of

Table 1. Some Physical, Thermal, and Mechanical Properties of ZrB₂ and HfB₂ Aerogels and Xerogels

sample	density (mg/cm ³)	% theoretical max. density	thermal conductivity (W/(m K))	Young's modulus (GPa)	hardness (MPa)
ZrB ₂ xerogel	881 ± 80	14.4	0.328 ± 0.010	0.81 ± 0.10	10.83 ± 0.63
HfB ₂ xerogel	1058 ± 100	9.5		2.71 ± 0.59	15.39 ± 0.87
ZrB ₂ aerogel	413 ± 40	6.7	0.184 ± 0.008	0.034 ± 0.0024	1.67 ± 0.17
HfB ₂ aerogel	407 ± 40	3.6		0.017 ± 0.006	0.90 ± 0.11

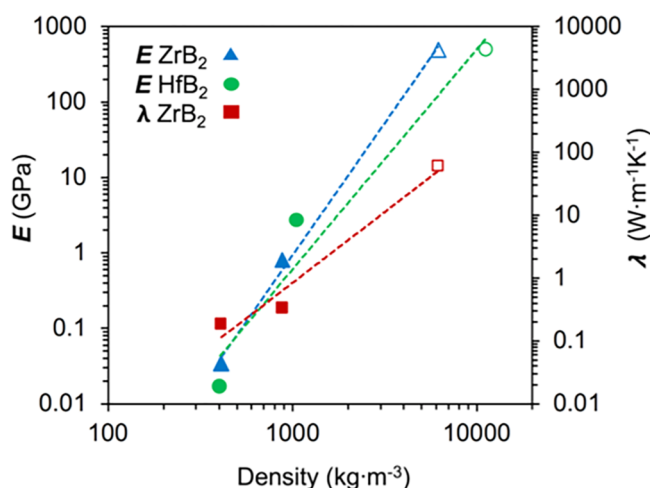
**Figure 3.** XRD spectra of HfB₂ and ZrB₂ aerogels.**Figure 4.** SEM images of (a, b) ZrB₂ aerogels. TEM images of (c) ZrB₂ and (d) HfB₂ aerogels.

large particles present after borothermal reduction, the vast majority of particles are less than 100 nm in diameter. Nitrogen porosimetry was also performed to determine the surface area of the ZrB₂ and HfB₂ aerogels, which is correlated with the primary particle size of the aerogel. BET surface areas of the ZrB₂ and HfB₂ aerogels were 19 and 10 m²/g, respectively. These surface area values suggest average particle sizes of 50 and 52 nm for ZrB₂ and HfB₂ aerogels, respectively, which are consistent with the sizes observed in SEM and TEM, as well as the crystallite sizes determined from XRD. The ZrB₂ and HfB₂ aerogels consist of particles with sizes similar to those observed in more traditional aerogels^{17–19} and much

smaller than those reported in previous works on UHTC materials.^{25–28}

Consistent with other material systems, there is a significant reduction in thermal conductivity between the aerogel and bulk forms. At ambient temperature, the conductivities for the ZrB₂ aerogels and xerogels are 0.184 ± 0.008 and 0.328 ± 0.010 W/(m K), respectively, more than 2 orders of magnitude (300 times) lower than the thermal conductivity of fully dense ZrB₂.¹⁶ This dramatic drop is typical of aerogel structures with ultrafine grains and porosity and has been demonstrated with other conductive materials, such as carbon,³⁰ and is a strong function of density. For reference, silica, a traditional aerogel material, experiences a 100 times reduction in thermal conductivity between dense and aerogel forms vs 300 times for ZrB₂.¹⁷ Figure 5 shows the thermal conductivity (λ) of ZrB₂ as a function of density (ρ)

$$\lambda \propto \rho^\alpha \quad (3)$$

**Figure 5.** Young's modulus (E) for ZrB₂ and HfB₂ aerogels and xerogels (left axis) and thermal conductivity (λ) for ZrB₂ aerogels and xerogels (right axis). The open data points represent ZrB₂ or HfB₂ properties at full density taken from the literature.¹⁶ Error bars are equal to or less than the size of the data symbols.

Power-law fits of the data give scaling exponents of $\alpha = 2.25 \pm 0.42$ for thermal conductivity of ZrB₂, which is slightly higher than that of carbon aerogels ($\alpha = 1.5$) but in the expected range. This superlinear dependence is what allows aerogels to perform so well as thermal insulators. Figure 5 also presents Young's modulus (E) of ZrB₂ and HfB₂ as a function of density (ρ)

$$E \propto \rho^\tau \quad (4)$$

The modulus is also observed to depend superlinearly on density. Power-law fits of the modulus data give scaling exponents of $\tau = 3.5 \pm 0.19$ and 2.92 ± 0.70 for ZrB₂ and HfB₂, respectively. The exponent values for both ZrB₂ and

HfB_2 are consistent with a form of irregular, fractal morphology ($\tau > 3$)^{17,31} and slightly higher than that of graphene-derived carbon aerogels ($\tau = 2.5$) produced by a similar method.³² Due to the lower hardness and Young's modulus values of these UHTC aerogels and xerogels, the final application for these thermal insulators would most likely include a dense skin to protect and structurally support the ultralow-density regime, similar to a space shuttle tile.

High-temperature survivability of a ZrB_2 aerogel was demonstrated by subjecting a monolith to 2000 °C for 30 min under flowing helium. Figure 6 shows that the monolith

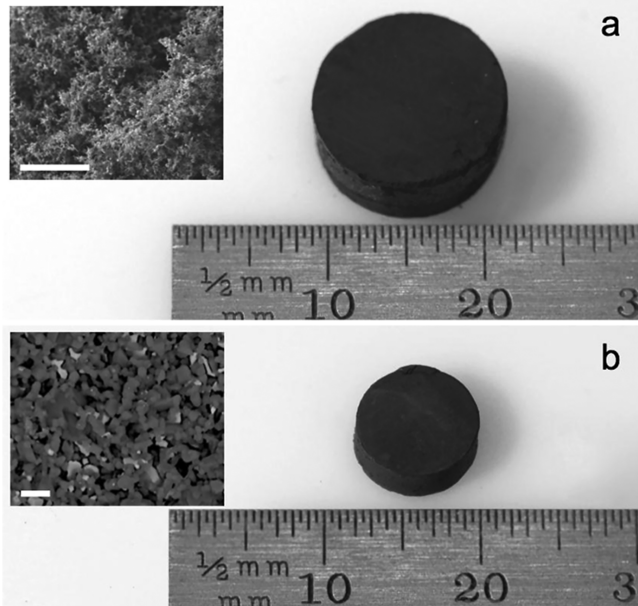


Figure 6. ZrB_2 aerogel (a) as-synthesized and (b) after 30 min at 2000 °C in an inert atmosphere. Inset: SEM images of the corresponding grain structure, scale bar = 5 μm .

maintains its form before (Figure 6a) and after (Figure 6b) heat treatment. There is some shrinkage on the order of 35% in addition to grain growth (inset), which is to be expected as fine-grained ZrB_2 is known to sinter at ambient pressure at around 2100 °C.³³ This type of high-temperature sintering could be used to increase the strength of these aerogels, potentially at the cost of increased thermal conductivity from particle coarsening. The beauty of the sol–gel synthesis process is its flexibility; UHTC materials could be made with tailorabile densities and compositions to best match the thermal and mechanical requirements of the final design. This novel combination of high melting temperature and ultralow thermal conductivity is demonstrated by the Ashby-type diagram in Figure 7, which shows how the UHTC aerogels stand apart from other material candidates for high-temperature applications.

CONCLUSIONS

By adjusting precursor chemistry and taking advantage of the borothermal reduction process, the realm of aerogels can be extended to UHTC materials. $\text{B}-\text{MO}_2$ aerogel monoliths were produced from epoxide-initiated gelation of ethanolic solutions of metal salts with suspended boron nanoparticles. These aerogel precursors were fired to produce low-density, highly porous MB_2 samples via a borothermal reduction of the metal

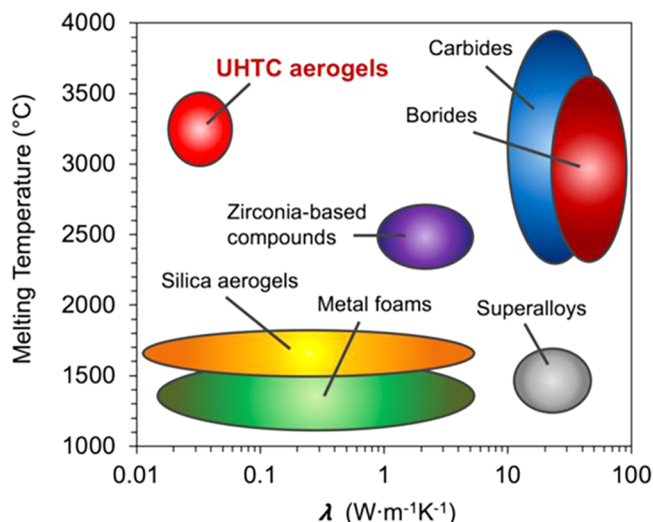


Figure 7. Unique position of UHTC aerogels in an Ashby-type diagram of the melting temperature vs thermal conductivity for multiple classes of high-temperature materials.

oxide. XRD confirms the presence of the MB_2 phase and an absence of unreacted boron, boron oxide, or metal oxide. The relative densities of the HfB_2 and ZrB_2 aerogels are 3 and 7%, respectively, with constituent particles less than 100 nm in size. The aerogels exhibited surface areas of $>10 \text{ m}^2/\text{g}$ and thermal conductivities as low as 0.184 W/(m K). The relative density of the boride aerogels can be tailored by adjusting reagent concentrations and the drying conditions, and due to the flexibility of the sol–gel chemistry and abundance of metal salts, this synthesis process could easily be expanded to produce other metal boride and carbide aerogels.

AUTHOR INFORMATION

Corresponding Author

*E-mail: worsley1@llnl.gov.

ORCID

James T. Cahill: [0000-0002-1555-6779](https://orcid.org/0000-0002-1555-6779)

Sally Turner: [0000-0003-0618-5133](https://orcid.org/0000-0003-0618-5133)

Jianchao Ye: [0000-0001-8939-0612](https://orcid.org/0000-0001-8939-0612)

Notes

The authors declare no competing financial interest.

ACKNOWLEDGMENTS

This work was performed under the auspices of the U.S. Department of Energy by Lawrence Livermore National Laboratory under Contract DE-AC52-07NA27344. This work was also supported in part by the Director, Office of Science, Office of Basic Energy Sciences, Materials Sciences and Engineering Division, of the U.S. Department of Energy under Contract No. DE-AC02-05-CH11231, within the sp²-Bonded Materials Program (KC2207), which provided for TEM characterization. Work at the Molecular Foundry was supported by the Office of Science, Office of Basic Energy Sciences, of the U.S. Department of Energy under Contract No. DE-AC02-05-CH11231. Funding was additionally provided by the Air Force Office of Scientific Research under Award No. FA9550-14-1-0323, which provided for materials. This work was also funded by the Laboratory Directed Research and Development (LDRD) program at Lawrence

Livermore National Laboratory (19-DR-002). S.T. acknowledges support from an NSF GFRFP fellowship.

■ REFERENCES

- (1) ASM Handbook. *Alloy Phase Diagrams*; ASM International, 1992; Vol. 3, pp 2–319.
- (2) Gild, J.; Zhang, Y.; Harrington, T.; Jiang, S.; Hu, T.; Quinn, M. C.; Mellor, W. M.; Zhou, N.; Vecchio, K.; Luo, J. High-Entropy Metal Diborides: A New Class of High-Entropy Materials and a New Type of Ultrahigh Temperature Ceramics. *Sci. Rep.* **2016**, *6*, No. 37946.
- (3) Li, H.; Yao, D.; Fu, Q.; Liu, L.; Zhang, Y.; Yao, X.; Wang, Y.; Li, H. Anti-oxidation and ablation properties of carbon/carbon composites infiltrated by hafnium boride. *Carbon* **2013**, *52*, 418–426.
- (4) Zoli, L.; Sciti, D. Efficacy of a ZrB_2 –SiC matrix in protecting C fibres from oxidation in novel UHTCMC materials. *Mater. Des.* **2017**, *113*, 207–213.
- (5) Meléndez-Martínez, J. J.; Domínguez-Rodríguez, A.; Monteverde, F.; Melandri, C.; De Portu, G. Characterisation and high temperature mechanical properties of zirconium boride-based materials. *J. Eur. Ceram. Soc.* **2002**, *22*, 2543–2549.
- (6) Opeka, M. M.; Talmy, I. G.; Wuchina, E. J.; Zaykoski, J. A.; Causey, S. J. Mechanical, thermal, and oxidation properties of refractory hafnium and zirconium compounds. *J. Eur. Ceram. Soc.* **1999**, *19*, 2405–2414.
- (7) Zapata-Solvias, E.; Jayaseelan, D. D.; Lin, H.-T.; Brown, P.; Lee, W. E. Mechanical properties of ZrB_2 - and HfB_2 -based ultra-high temperature ceramics fabricated by spark plasma sintering. *J. Eur. Ceram. Soc.* **2013**, *33*, 1373–1386.
- (8) Chamberlain, A. L.; Fahrenholtz, W. G.; Hilmas, G. E.; Ellerby, D. T. High-strength zirconium diboride-based ceramics. *J. Am. Ceram. Soc.* **2004**, *87*, 1170–1172.
- (9) Monteverde, F.; Guicciardi, S.; Bellosi, A. Advances in microstructure and mechanical properties of zirconium diboride based ceramics. *Mater. Sci. Eng., A* **2003**, *346*, 310–319.
- (10) Post, B.; Glaser, F. W.; Moskowitz, D. Transition metal diborides. *Acta Metall.* **1954**, *2*, 20–25.
- (11) Norasetthekul, S.; Eubank, P. T.; Bradley, W. L.; Bozkurt, B.; Stucker, B. Use of zirconium diboride-copper as an electrode in plasma applications. *J. Mater. Sci.* **1999**, *34*, 1261–1270.
- (12) Opeka, M. M.; Talmy, I. G.; Zaykoski, J. A. Oxidation-based materials selection for 2000 C+ hypersonic aerosurfaces: theoretical considerations and historical experience. *J. Mater. Sci.* **2004**, *39*, 5887–5904.
- (13) Van Wie, D. M.; Drewry, D. G.; King, D. E.; Hudson, C. M. The hypersonic environment: required operating conditions and design challenges. *J. Mater. Sci.* **2004**, *39*, 5915–5924.
- (14) Cutler, R. *Engineering Properties of Borides*, Engineered Materials Handbook; ASM International, 1991; Vol. 4, pp 787–803.
- (15) Zimmermann, J. W.; Hilmas, G. E.; Fahrenholtz, W. G.; Dinwiddie, R. B.; Porter, W. D.; Wang, H. Thermophysical properties of ZrB_2 and ZrB_2 –SiC ceramics. *J. Am. Ceram. Soc.* **2008**, *91*, 1405–1411.
- (16) Fahrenholtz, W. G.; Hilmas, G. E.; Talmy, I. G.; Zaykoski, J. A. Refractory diborides of zirconium and hafnium. *J. Am. Ceram. Soc.* **2007**, *90*, 1347–1364.
- (17) Lu, X.; Arduini-Schuster, M. C.; Kuhn, J.; Nilsson, O.; Fricke, J.; Pekala, R. W. Thermal conductivity of monolithic organic aerogels. *Science* **1992**, *255*, 971–972.
- (18) Neugebauer, A.; Chen, K.; Tang, A.; Allgeier, A.; Glicksman, L. R.; Gibson, L. J. Thermal conductivity and characterization of compacted, granular silica aerogel. *Energy Build.* **2014**, *79*, 47–57.
- (19) Smith, D. M.; Maskara, A.; Boes, U. Aerogel-based thermal insulation. *J. Non-Cryst. Solids* **1998**, *225*, 254–259.
- (20) Kuntz, J. D.; Cervantes, O. G.; Gash, A. E.; Munir, Z. A. Tantalum–tungsten oxide thermite composites prepared by sol–gel synthesis and spark plasma sintering. *Combust. Flame* **2010**, *157*, 1566–1571.
- (21) Gash, A. E.; Tillotson, T. M.; Satcher, J. H., Jr.; Poco, J. F.; Hrubesh, L. W.; Simpson, R. L. Use of epoxides in the sol–gel synthesis of porous iron (III) oxide monoliths from Fe (III) salts. *Chem. Mater.* **2001**, *13*, 999–1007.
- (22) Lecomte, A.; Blanchard, F.; Dauger, A.; Silva, M. C.; Guinebretiere, R. Synthesis and sintering of zirconium oxide aerogel. *J. Non-Cryst. Solids* **1998**, *225*, 120–124.
- (23) Sun, Q.; Zhang, Y.; Deng, J.; Chen, S.; Wu, D. A novel preparation process for thermally stable ultrafine tetragonal zirconia aerogel. *Appl. Catal., A* **1997**, *152*, L165–L171.
- (24) Kidchob, T.; Malfatti, L.; Serra, F.; Falcaro, P.; Enzo, S.; Innocenzi, P. Hafnia sol-gel films synthesized from $HfCl_4$: Changes of structure and properties with the firing temperature. *J. Sol-Gel Sci. Technol.* **2007**, *42*, 89–93.
- (25) Guo, W.-M.; Yang, Z.-G.; Zhang, G.-J. Synthesis of submicrometer HfB_2 powder and its densification. *Mater. Lett.* **2012**, *83*, 52–55.
- (26) Guo, W. M.; Zhang, G. J. New borothermal reduction route to synthesize submicrometric ZrB_2 powders with low oxygen content. *J. Am. Ceram. Soc.* **2011**, *94*, 3702–3705.
- (27) Guo, W. M.; Zhang, G. J.; You, Y.; Wu, S. H.; Lin, H. T. TiB_2 powders synthesis by borothermal reduction in TiO_2 under vacuum. *J. Am. Ceram. Soc.* **2014**, *97*, 1359–1362.
- (28) Wu, H.; Yin, J.; Liu, X.; Huang, Z.; Lee, S.-H. Aqueous gelcasting and pressureless sintering of zirconium diboride foams. *Ceram. Int.* **2014**, *40*, 6325–6330.
- (29) Gregg, S.; Sing, K. S. W. *Adsorption, Surface Area and Particles Migrate into the Carbon Matrix. The Migration of Porosity*; Academic Press: London, 1982.
- (30) Worsley, M. A.; Satcher, J. H., Jr.; Baumann, T. F. Enhanced thermal transport in carbon aerogel nanocomposites containing double-walled carbon nanotubes. *J. Appl. Phys.* **2009**, *105*, No. 084316.
- (31) Lu, X.; Nilsson, O.; Fricke, J.; Pekala, R. W. Thermal and electrical conductivity of monolithic carbon aerogels. *J. Appl. Phys.* **1993**, *73*, 581–584.
- (32) Worsley, M. A.; Charnvanichborikarn, S.; Montalvo, E.; Shin, S. J.; Tyłski, E. D.; Lewicki, J. P.; Nelson, A. J.; Satcher, J. H., Jr.; Biener, J.; Baumann, T. F.; Kucheyev, S. O. Toward Macroscale, Isotropic Carbons with Graphene-Sheet-Like Electrical and Mechanical Properties. *Adv. Funct. Mater.* **2014**, *24*, 4259–4264.
- (33) Chamberlain, A. L.; Fahrenholtz, W. G.; Hilmas, G. E. Pressureless sintering of zirconium diboride. *J. Am. Ceram. Soc.* **2006**, *89*, 450–456.